

Coarsening of Inter- and Intra-granular Proeutectoid Cementite in an Initially Pearlitic 2C-4Cr Ultrahigh Carbon Steel



MATTHEW D. HECHT, YOOSUF N. PICARD, and BRYAN A. WEBLER

We have examined spheroidization and coarsening of cementite in an initially pearlitic 2C-4Cr ultrahigh carbon steel containing a cementite network. Coarsening kinetics of spheroidized cementite and growth of denuded zones adjacent to the cementite network were investigated by analyzing particle sizes from digital micrographs of water-quenched steel etched with Nital. Denuded zones grew at a rate proportional to $t^{1/4}-t^{1/5}$. Spheroidization of pearlite was completed within 90 minutes at 1073 K and 1173 K (800 °C and 900 °C), and within 5 minutes at 1243 K (970 °C). Bimodal particle size distributions were identified in most of the samples and were more pronounced at higher temperatures and hold times. Peaks in the distributions were attributed to the coarsening of intragranular and grain boundary particles at different rates. A third, non-coarsening peak of particles was present at 1073 K (800 °C) only and was attributed to particles existing prior to the heat treatment. Particle sizes were plotted vs time to investigate possible coarsening mechanisms. The coarsening exponent for the growth of grain boundary carbides was closest to 4, indicating grain boundary diffusion control. The coarsening exponent was closest to 5 for intragranular carbides, indicating suppression of volumetric diffusion (possibly due to reduced effective diffusivity because of Cr alloying) and control by dislocation diffusion.

DOI: 10.1007/s11661-017-4012-2

© The Minerals, Metals & Materials Society and ASM International 2017

I. INTRODUCTION

A. Ultrahigh Carbon Steels

ULTRAHIGH carbon steels (UHCS) have been used for many years in various applications demanding high strength and excellent wear resistance. UHCS are hypereutectoid steels with carbon contents in the range of 1.0 to 2.1 wt pct. As a result of this high C content, there is precipitation of proeutectoid cementite (Fe_3C) during cooling from casting and/or during heat treatment processes. The hard and brittle cementite contributes to the high hardness and wear resistance of UHCS, which is desirable for applications involving the cutting or shaping of other metals. UHCS have been used in rolling mills as far back as 1913^[1] and are also commonly used in tool steels. There has been interest over the last few decades in using UHCS for other applications where traditionally lower carbon content steels have been utilized, such as sheet and automotive steels.^[2,3]

Eutectoid and proeutectoid cementite in UHCS tend to form a network along austenite grain boundaries, which provides crack initiation sites and propagation pathways. Toughness decreases as a function of network connectivity, plateauing once a critical network

connectivity is reached.^[4] The network is surrounded by a matrix made up of eutectoid transformation products, such as pearlite (lamellar eutectoid cementite + ferrite), bainite, and/or martensite. The matrix strongly affects steel hardness and may also influence toughness. Studies indicate that low toughness in UHCS can be mitigated through network breakup by microalloying^[5-7] or thermomechanical processing.^[8]

UHCS are typically heat treated after casting to improve mechanical properties. Heating a pearlitic matrix to near or above the eutectoid temperature will cause spheroidization of cementite lamellae into equiaxed particles. Further time at temperature will result in curvature-driven particle coarsening. Carbide particle size distribution influences fracture toughness^[9] and yield strength,^[10] and potentially also the proeutectoid network volume fraction and connectivity in UHCS. Gurland^[11] noted that cracking in tension and torsion in spheroidized pearlite tended to occur in the largest cementite particles. A smaller mean free path between particles, *i.e.*, a smaller particle size, typically improves both toughness and hardness, so processing to produce a finer distribution of particles is usually beneficial. On the other hand, a partially pearlitic microstructure might be desirable for increased wear resistance.^[12] Closely spaced particles are more likely to lead to a non-lamellar divorced eutectoid transformation upon cooling from the austenite.^[13] Thus, understanding particle coarsening behavior is desirable for improving the tailoring of mechanical properties *via* heat treatment processes for UHCS.

MATTHEW D. HECHT, YOOSUF N. PICARD, and BRYAN A. WEBLER are with the Department of Materials Science and Engineering, Carnegie Mellon University, 5000 Forbes Avenue, Pittsburgh, PA 15213. Contact e-mail: webler@cmu.edu

Manuscript submitted December 3, 2016.

Article published online February 21, 2017

B. Kinetics of Particle Coarsening

In 1961 Lifshitz and Slyozov^[14] and Wagner^[15] independently derived a mathematical treatment of coarsening of small volumes of dilute second phase particles by bulk diffusion (LSW theory). In LSW theory, each particle sees a concentration gradient field based on the curvature of all other particles. The radius of curvature r of a particle affects the concentration of solute in the matrix C_r immediately surrounding it according to the Gibbs–Thomson Equation:^[16]

$$C_r = C_\infty + 2\sigma V_m / RT r$$

C_∞ is the equilibrium matrix concentration, V_m is the molar volume of the precipitate, R is the gas constant, and T is the temperature. Differences in particle curvatures result in concentration gradients from small particles to larger particles. The result is that particles above a critical radius grow and those below it shrink. In a random and dilute distribution of particles, the critical radius is the mean particle size.

The general form of the coarsening equation is:

$$r^n - r_0^n = k_n(t - t_0),$$

where r is the mean particle radius at time t , r_0 and t_0 are the mean radius and time at the start of steady-state coarsening, respectively, and k_n is a temperature (T)-dependent constant and n depends on the diffusive mechanism controlling particle coarsening: $n = 3$ for bulk/volume diffusion; $n = 4$ for grain boundary diffusion; $n = 5$ for dislocation diffusion.

The LSW derivation considered bulk diffusion only, and predicted that particle coarsening would proceed according to time to the 1/3 power, such that:

$$r^3 - r_0^3 = k_3(t - t_0).$$

The constant k_3 in this equation includes the diffusion coefficient D , surface energy γ , equilibrium solute concentration C_0 , and molar volume V_m of the coarsening phase:

$$k_3 = \frac{8\gamma DC_0 V_m^2}{9RT}$$

Speight^[17] extended the theory to include microstructures where two-dimensional diffusion along grain boundaries was dominant:

$$r^4 - r_0^4 = k_4(t - t_0).$$

k_4 is similar to k_3 but depends on grain boundary energies and diffusion coefficient. Ardell^[18] extended the theory to include systems where diffusion along dislocations was dominant:

$$r^5 - r_0^5 = k_5(t - t_0).$$

Particle diameter (d) may be used instead of particle radius (r) in these equations if an extra factor of 2^n is

multiplied into k . It has been theorized^[19] that systems may have combined diffusion mechanisms in operation such that

$$r \propto \left(at + bt^{3/4} + ct^{3/5} \right)^{1/3}.$$

The constants a , b , and c scale the contribution of each diffusive mechanism. Thus, the coarsening exponent n might take on non-integer values between 3 and 5 depending on the contributions of each mechanism to the overall coarsening process.

Identifying the n value for a given coarsening process can pose a challenge. Typically, mean particle diameters are plotted vs time on a log-scale plot, and n and k are extracted from the equation for the best fit line:

$$\log(d) = \frac{1}{n} \cdot \log(kt)$$

This procedure is applicable if the initial particle size d_0 is negligible. If d_0 is not negligible, then unless $k \cdot t_0 = d_0^n$ the apparent value of n will be different from the true n value when extracted from a log–log plot.

The literature regarding cementite coarsening in steel considers two general cases: coarsening of cementite produced during tempering of supersaturated martensite^[20–22] and coarsening of spheroidized pearlite particles.^[23–25] The literature n values for various steels ranged from about 2 to 6 (See Table I). Some of these n values may be erroneously high due to failure to correct for a non-negligible d_0 , especially in cases dealing with coarsening of the products of spheroidization.

The literature generally uses an effective diffusion coefficient in describing coarsening derived by Li *et al.*^[26] for plain carbon steel reflecting constraints that cementite composition and volume remain constant during coarsening:

$$D_{\text{eff}} = \frac{C_{\text{Fe}} D_{\text{Fe}} D_{\text{C}} V_{\text{Fe}}^2 + C_{\text{C}} D_{\text{Fe}} D_{\text{C}} V_{\text{C}} V_{\text{Fe}}}{C_{\text{Fe}} D_{\text{Fe}} V_{\text{Fe}}^2 + C_{\text{C}} D_{\text{C}} V_{\text{C}}^2}$$

C_{Fe} and C_{C} refer to the concentrations of iron and carbon, respectively. V_{Fe} is the atomic volume of Fe and V_{C} is the difference between the volume of one molecule of Fe_3C and three atoms of iron in ferrite (or austenite). In steels with significant Cr alloying, Cr is reported to substitute for Fe in cementite up to about 18 wt pct.^[27] Due to the constant composition constraint, the expression for the effective diffusion coefficient should be modified to hold the Cr composition constant. While the diffusion coefficient of Cr in Fe is very close to the self-diffusion coefficient of Fe, the concentration of Cr is overall significantly lower. Cr alloying has also been suggested to increase the activation energy of iron self-diffusion, though its effect is not well understood.^[28] Thus, the effective diffusion coefficient controlling cementite coarsening might be significantly lowered by Cr alloying leading to substantially slower coarsening. Zhang *et al.*^[29] in a study of an initially pearlitic 1 wt pct C steel observed that “the addition of substitutional

Table I. Literature References for n Values in Cementite Coarsening

Year	C and Cr	Temperatures [K (°C)]	n Value	References
1968	0.3C	948 (675), 993 (720)	3 to 4	25
1982	0.33C	903 to 963 (630 to 690)	2.7 to 3.0	20
1995	1C-1.5Cr	973 to 1013 (700 to 740)	2.9 to 3.0	23
1998	0.2 to 1.4C	963 (690)	4.3 to 5.0	19
1999	0.45-C	973 (700)	3.7 to 4.4	22
2008	0.8C	973 (700)	4.1 to 6.1	24
2008	0.8C-1Cr	973 (700)	2.0 to 6.3	24

alloying elements (Mn, Si, Cr) can remarkably retard the coarsening of cementite particles.”

Some authors found changes in the slope of r vs t . Day and Barford^[25] noted an abrupt change in slope in their r vs t data corresponding to a change in n values from 3 to 4 at about 20,000 seconds at 948 K (675 °C), which they attributed to a change in the dominant coarsening mechanism from bulk diffusion to grain boundary diffusion. Cree *et al.*^[23] noted very high n values before about 3600 seconds at 1013 K (740 °C) and 10,000 seconds at 973 K (700 °C), which they attributed to an initial “transient” period of particle growth, after which they observed $n \sim 3$ indicating bulk diffusion-controlled coarsening. Nam and Bae^[22] reported that grain boundary particles were coarsened with $n \sim 4.5$, while intragranular particles were coarsened with $n \sim 3.7$.

In the existing literature on cementite coarsening in steels, the maximum carbon concentration studied was 1.4 wt pct C, the maximum chromium concentration studied was 1.5 wt pct Cr, and the maximum temperature studied was 1013 K (740 °C). The present study analyzes cementite coarsening kinetics in a new regime of chemistry and temperature: 2 wt pct carbon, 4 wt pct Cr between 1073 K and 1243 K (800 °C and 970 °C). The high chromium content is of interest because it might lead to slower coarsening kinetics by lowering the effective diffusion coefficient. The high carbon concentration is of interest because of the resulting cementite network. The effects of the network on coarsening kinetics and the effects of the coarsening heat treatments on the network have not been studied previously.

II. MATERIALS AND METHODS

Sections of 36-inch diameter centrifugally cast UHCS mill rolls cut by band saw were provided for this study by Miller Centrifugal Casting (MCC). Different samples of as-cast UHCS (composition shown in Table II) about 1cm on each side were placed in a preheated box furnace at 1073 K, 1173 K, and 1243 K (800 °C, 900 °C, and 970 °C) for times of 5 minutes, 90 minutes, 3 hours, 8 hours, and 24 hours, and then quenched in water at room temperature. All of these heat treatments were in the two-phase austenite + cementite/(Fe,Cr)₃C phase field according to Thermo-Calc calculations (version 2016b, TCFE8 database).^[30] An additional heat treatment of 85 hours at 1073 K (800 °C) was also conducted.

Since heat treatments were conducted in air, we ensured microstructural analysis avoided the decarburized region. The greatest potential depth of decarburization for these heat treatments was calculated at about 3 mm for 24 hours at 1243 K (970 °C).^[31] All samples were more than twice as large as this depth and the decarburized zone was avoided during microstructural characterization by imaging close to the center of the samples.

Heat-treated samples were cross sectioned along the midline with a water-cooled alumina cutoff wheel, then were polished with 1 μ m alumina and etched for 25 to 30 seconds in 4 to 5 pct Nital (nitric acid in ethanol). Etched samples were imaged using a Phillips XL-30 scanning electron microscope (SEM) at 20 kV accelerating voltage in secondary electron imaging mode. The resulting micrographs were then analyzed using the public domain ImageJ software.^[32]

To investigate coarsening kinetics, we developed a specialized particle analysis methodology in ImageJ that quantified particle sizes from multiple digital micrographs. The core steps of the method are shown in Figure 1. This method was used for all samples except for the 5-minute holds at 1073 K and 1173 K (800 °C and 900 °C). The method was not suitable for those two samples because they were partially pearlitic and particles could not be properly targeted and isolated by the edge detection filter because of the cementite lamellae. At least 2000 particles were analyzed per heat treat condition except in the case of the aforementioned two samples, for which 102 particles [1073 K (800 °C), 5 minute hold] and 321 particles [1173 K (900 °C), 5-minute hold] were measured by manually fitting ellipses to particles. Particle areas (A) were measured in all cases, and diameters were calculated assuming spherical particles such that $d = 2\sqrt{A/\pi}$. Corrections for stereology were made according to Saltikov’s procedure:^[33] logarithms of the diameters were taken, then sorted into bins (size classes) of 0.1 log (μ m), from -1.2 (0.06 μ m) to 0.8 (6.3 μ m). The number of particles within each bin was then corrected to account for stereology according to the following expression:

$$N_{Vi} = \alpha_1 N_{Ai} - \sum_{j=1}^{i-1} \alpha_{j+1} N_{A(i-j)},$$

where N_{Vi} is the number of particles in the i th bin corrected for stereology, N_{Ai} is the number of particles in the i th bin before correction, and α_i are constants. Errors due to the assumption of perfectly spherical

Table II. As-cast UHCS Composition in Weight Percent

C	Si	Mn	Cr	Ni	Mo
2.02	0.65	0.72	3.86	1.45	0.33

Carbon content measured by combustion analysis, other elements by ICP-OES (inductively coupled plasma optical emission spectrometry).

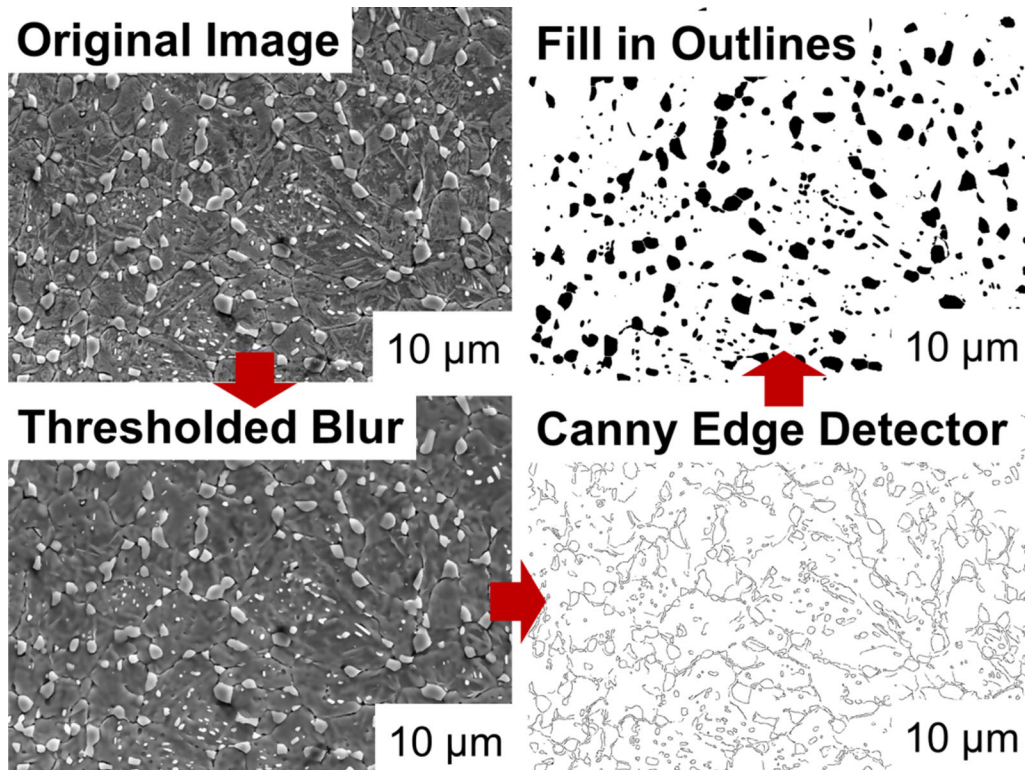


Fig. 1—Steps in the particle analysis methodology using ImageJ to quantify carbide particle sizes. First a thresholded blur filter was applied to the original digital SEM micrograph to smooth contrast outside the particles. Next, application of a Canny edge detection algorithm identified particle edges. Finally, particle outlines were filled in and a 2-pixel width median filter was applied to remove non-particle edges.

particles should not be significant since the aspect ratios of the particles were not large.^[34]

III. RESULTS

The initial (as-cast) microstructure consisted of a network of cementite surrounded by a matrix of pearlite as shown by the SEM micrograph in Figure 2. Upon heating, the pearlite matrix spheroidized into discrete particles that coarsened over time at rates dependent on temperature. Particles were uniformly distributed in the matrix, with the exception of denuded zones free of particles adjacent to the cementite network. These zones were found to grow in size with greater annealing time.

A. Denuded Zone Widths Next to Cementite Network

Denuded zone widths next to network branches were measured for various times and temperatures. Figure 3(a) shows an example of a branch of the cementite network with a denuded zone, and

Figure 3(b) shows the method used to quantify zone widths. For each time and temperature combination, zone widths next to five different branches in different areas of the network were measured. Average network branch widths and area fractions remained about the same over time, indicating that the denuded zones were not caused by network dissolution. Figure 4 shows the time evolution of denuded zone widths, which demonstrated an apparent power law relation with time:

$$d^n = kt.$$

The values of n for denuded zone growth are summarized in Table III. n values appeared to be around 4 or 5 for 1243 K or 1173 K (970 °C or 900 °C). An n value in the range of 4 to 5 was found at 1073 K (800 °C) for times up to 24 hours [1073 K (800 °C) (a) entry in Table III], but inclusion of data from a measurement at 85 hours at 1073 K (800 °C) changed n to around 9 for that temperature [1073 K (800 °C) (b) entry in Table III; $n=5$ was still within the range of error].

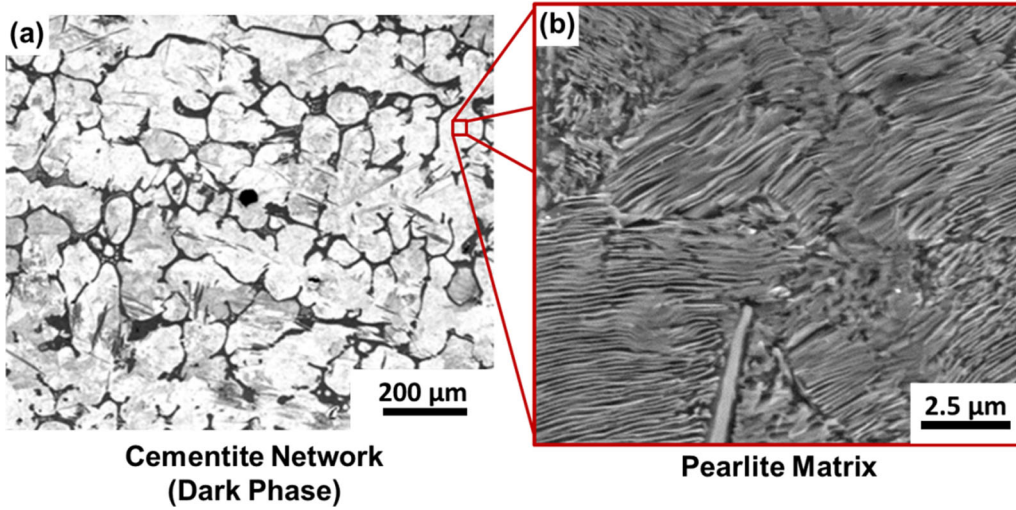


Fig. 2—SEM micrographs of the initial UHCS microstructure showing (a) a cementite network on prior austenite grain boundaries surrounded by (b) a pearlite matrix.

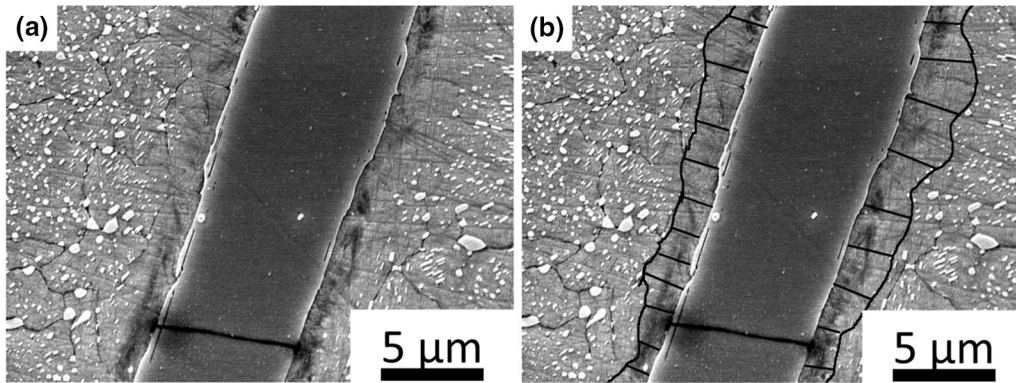


Fig. 3—SEM micrograph of (a) a branch of the cementite network on an original austenite grain boundary, which was (b) analyzed to find the average width of the denuded zone around it.

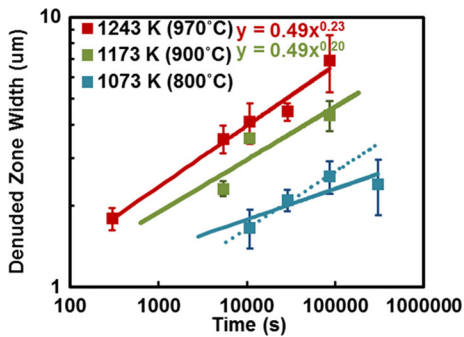


Fig. 4—Denuded zone widths vs time for heat treatments at three temperatures. The dotted blue line trend line for the 1073 K (800 °C) data (Entry 1073 (a) in Table III) neglects the data point at 85 h which might be affected by decarburization. The solid blue line includes the 85 h data point (Entry 1073 K (800 °C) (b) in Table III).

B. Particle Size Distributions

Representative areas of SEM micrographs of UHCS samples from each hold time and annealing temperature

Table III. *n* Values for Growth of Denuded Zones

Temperature	<i>n</i>
1243 K (970 °C)	4.4 ± 0.4
1173 K (900 °C)	5 ± 3
1073 K (800 °C) (a)	4.7 ± 0.4
1073 K (800 °C) (b)	9 ± 4

combination are shown in Figure 5. These areas correspond to the spheroidized microstructures well away from the proeutectoid cementite network and associated denuded zones discussed in the previous section. It was apparent that cementite particle sizes increased with temperature and hold time. There also appeared to be a bimodal particle size distribution at moderate annealing times, most readily apparent in Figures 5(h) and (l). Pearlite spheroidization was fully completed within 5 minutes at 1243 K (970 °C) (Figure 5(k)), and within 90 minutes at 1073 K and 1173 K (800 °C and 900 °C) as shown in Figures 5(b) and (g). Particles appeared to grow larger over time at each hold temperature.

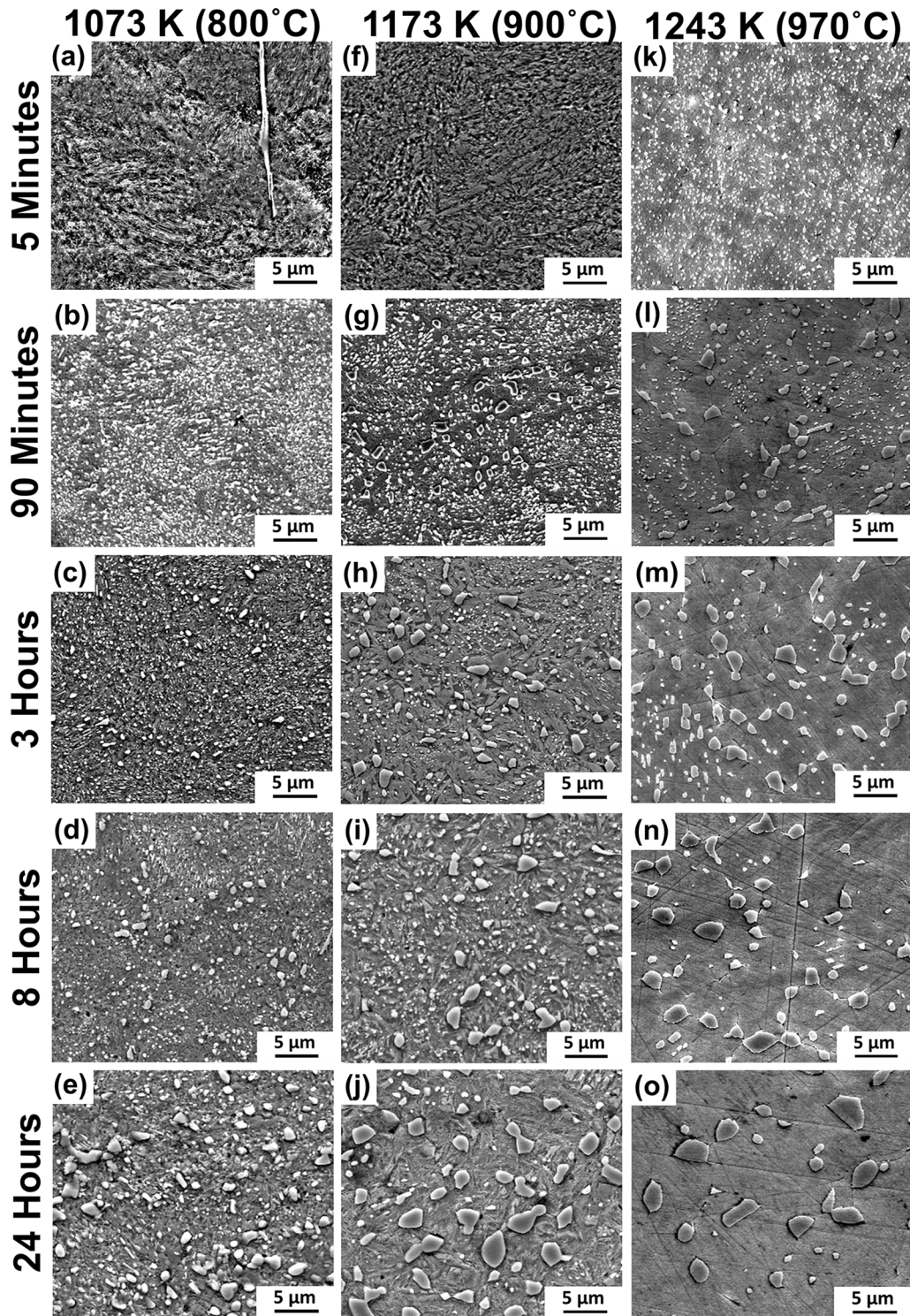


Fig. 5—SEM micrographs of UHCS microstructures of each (a) through (o) time and temperature combination ranging from 1073 K to 1243 K (800 °C to 970 °C) and 5 min to 24 h.

Digital micrographs of the UHCS microstructures shown in Figure 5 were quantitatively analyzed to find particle sizes using the methodology outlined in Figure 1. Plots of particle size distributions corrected for stereology are shown in Figure 6. Particle size distributions were log-normal in all cases, as is common

for particle analysis.^[35,36] Gaussian peak profiles were fit to the data by manually adjusting peak amplitude, width, and position to match the data as closely as possible. Nearly all of the measured distributions required at least two separate Gaussian profiles to fit the data. This was consistent with the distribution of

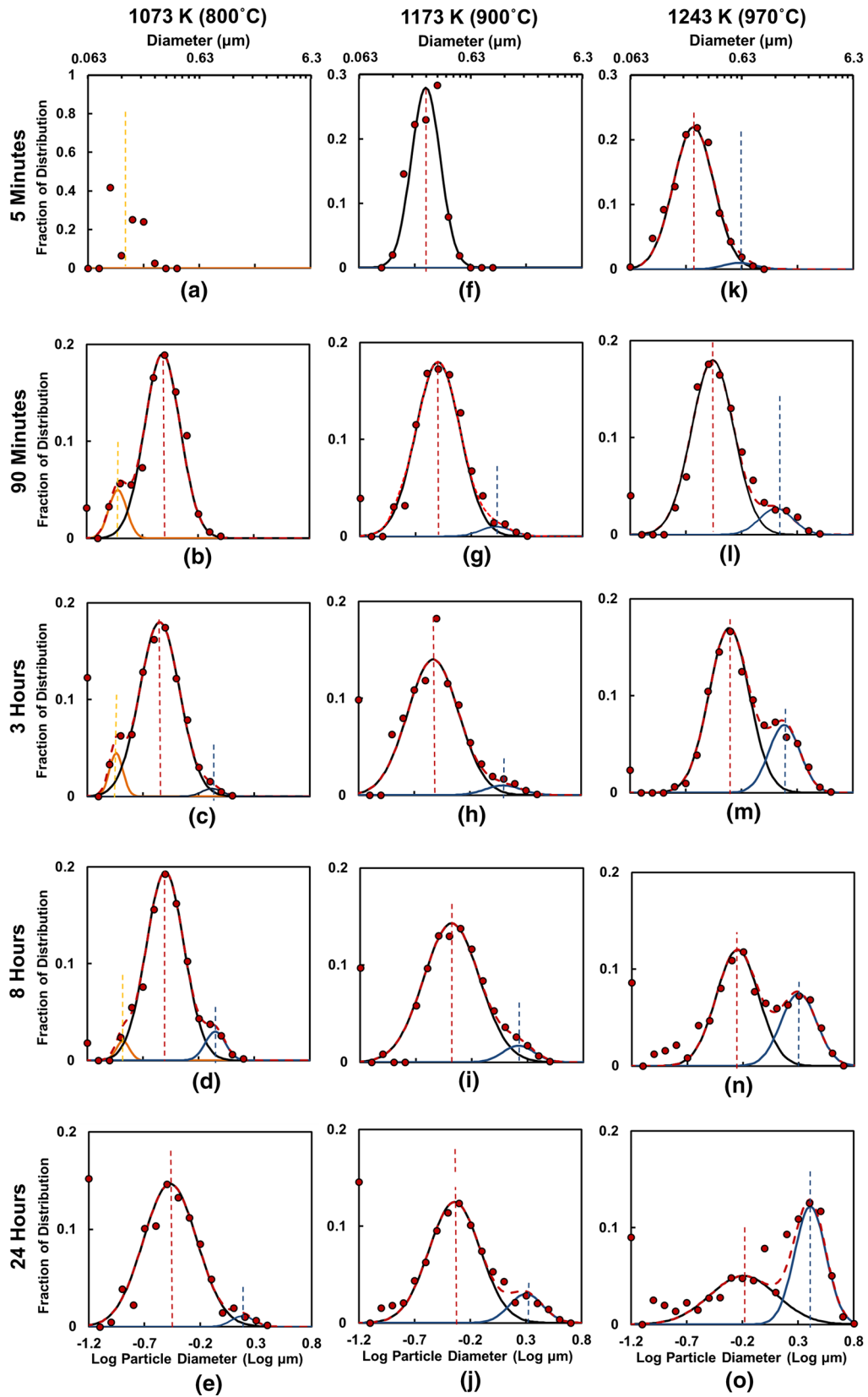


Fig. 6—Log particle size distributions of each (a) through (o) time and temperature combination ranging from 1073 K to 1243 K (800 °C to 970 °C) and 5 min to 24 h. Multiple peaks within the distributions were fit with Gaussian profiles. The dashed vertical lines in the figures denote the positions of the Gaussian profiles.

particles observed in, *e.g.*, Figure 5(m). A vertical dashed line denotes the peak position of each component distribution on the plots. The vertical line in Figure 6(a) is at the position of the mean of the particle size data since a Gaussian peak could not be fitted for 5 minutes at 1073 K (800 °C) data.

The feature common to every plot except for 5 minutes at 1073 K (800 °C) was a central distribution with its peak located around $-0.5 \log(\mu\text{m})$, or about $0.3 \mu\text{m}$. The position of that peak shifted to the right (larger particle sizes) over time at 1173 K and 1243 K (900 °C and 970 °C), but stayed fixed with time at 1073 K (800 °C). Two other peaks appeared in some of the samples: one to the left of the central distribution at about $-0.9 \log(\mu\text{m})$, or $0.13 \mu\text{m}$, that was fixed in time and one to the right of the central distribution that shifted further to the right (larger particle sizes) with longer annealing time. The left peak was only observed in samples annealed at 1073 K (800 °C), Figures 6(a) through (d).

C. Identifying Component Distributions

The central distribution was produced directly by the spheroidization of pearlite inside the austenite grains. The only plot in which this peak did not appear was Figure 6(a). The absence of a central peak in the Figure 6(a) plot indicated that spheroidization had not progressed to the point where particles were distinguishable among the spheroidizing pearlite lamellae. Central peak particles will be termed intragranular particles (IG) for the remainder of this article.

The left distribution consisted of the smallest particles, and only appeared at the lowest temperature studied. The left distribution was present in Figure 6(a) even though pearlite spheroidization had not completed, so the distribution apparently corresponded to particles that were already present in the initial microstructure prior to the heat treatment. For instance, Figure 7 showed that some regions of the initial as-cast pearlite microstructure contained particles. Left peak particles will be termed leftover particles (LP) for the remainder of this article.

There were two possible explanations for the presence of these LP particles. First, they could have been

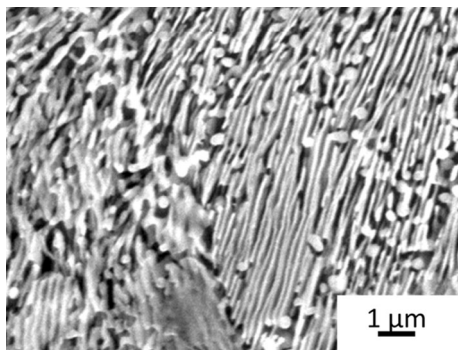


Fig. 7—SEM micrograph of as-cast UHCS showing a region of pearlite-containing particles, termed as leftover particles (LP).

spheroidized eutectoid cementite that formed *via* the divorced eutectoid transformation along with pearlite^[13] during cooling of the steel after casting. The LP particles may also have been $(\text{Fe,Cr})_{23}\text{C}_6$, a small amount of which was stable below the eutectoid temperature according to Thermo-Calc equilibrium calculations. The gradual disappearance of the left peaks in Figure 6 could be due to dissolution of the unstable M_{23}C_6 or divorced eutectoid cementite phase slowly dissolving at 1073 K (800 °C). The absence of the left peak at 1173 K and 1243 K (900 °C and 970 °C) was likely due to faster dissolution kinetics at those higher temperatures.

The right distribution was attributed to intergranular particle coarsening on austenite grain boundaries. Figure 8(a) shows a micrograph of UHCS heat treated for 8 hours at 1243 K (970 °C). The shapes of the cementite particles as well as some prior austenite grain boundaries revealed by the Nital etch enabled manual interpolation of the austenite grain boundary network (Figure 8(b)). The size distribution of all particles in seven such micrographs is shown in Figure 8(c), while the size distribution of the particles only at the grain boundaries in seven micrographs is shown in Figure 8(d). While the positions of the peaks did not change from Figures 8(c) through (d), the relative heights of the peaks changed significantly so as to nearly eliminate the central peak in the distribution. This indicated that particles on the grain boundaries contributed far more to the right distribution. The particles that comprise this right distribution will be termed grain boundary particles (GB) for the remainder of this article.

In some cases, grain boundary particles were present without showing an obvious second peak in the particle size distribution. Micrographs of a sample held at 1243 K (970 °C) for 5 minutes (example shown in Figure 9(a)) were traced along prior austenite grain boundaries revealed by Nital etching (Figure 9(b)). Initially, only a central peak was identified in the full particle size distribution in five such images (Figure 9(c)). When the distribution was modified to include only particles intersecting the grain boundaries, the result was that the distribution shifted to larger sizes as shown in Figure 9(d). It was not always possible to trace grain boundaries in every image, so some of the distributions with only a central peak potentially also contained an overlapped right peak.

IV. DISCUSSION

Annealing UHCS specimens above the austenitizing temperature showed a process of pearlite spheroidization into small size cementite particles followed by growth over time. The growth of the cementite particles over time showed evidence of coarsening at two different rates, resulting in a bimodal distribution of particles. These particles could be distinguished by their position relative to the prior austenite grain boundaries. As such, the dominant particle type by size transferred from

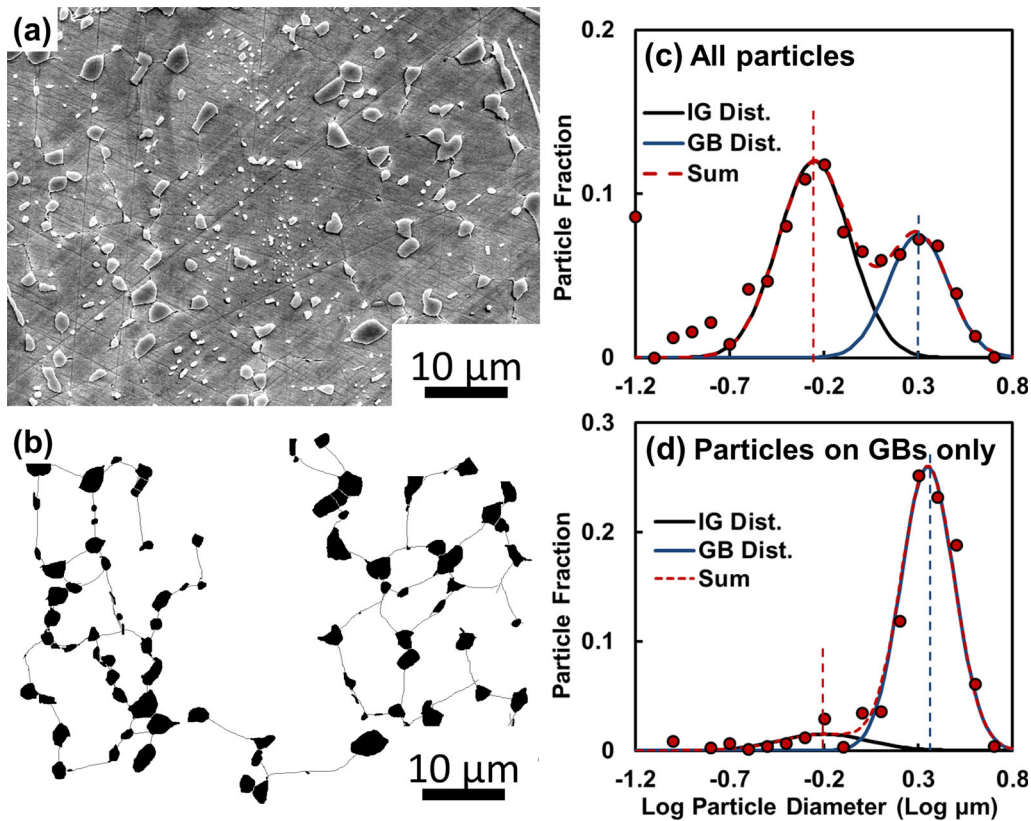


Fig. 8—Grain boundaries in (a) a micrograph of UHCS heat treated for 8 hours at 1243 K (970 °C) were (b) traced to isolate particles on grain boundaries. Particle size distributions are shown for (c) all particles and (d) only particles at the identified grain boundaries.

intragranular (IG) particles within grains to intergranular (GB) particles on grain boundaries. Concurrent to this observed particle coarsening behavior, cementite particles in the vicinity ($<10 \mu\text{m}$) of the proeutectoid cementite network dissolved to produce a “denuded” zone. This denuded zone extended further from the network boundary with longer annealing time. All of these observed carbide particle coarsening and dissolution processes exhibited a power law relationship. The associated kinetics of these processes is further discussed in the context of LSW theory.

A. Coarsening and Denuded Zone Growth Kinetics

As noted in Section III-B, denuded zones free of carbide particles formed adjacent to branches of the cementite network proportional to $t^{1/4}-t^{1/5}$. In the literature, precipitate-free zones (PFZ) next to normal grain boundaries grew at rates proportional to $t^{1/2}$.^[37,38] The growth of the denuded zones in this study was consistent with the particle coarsening kinetics. In UHCS, the branches of the proeutectoid cementite network may be viewed as very large particles with essentially zero curvature compared to cementite particles formed during the heat treatment (see Figure 3). Therefore, a curvature-driven concentration gradient from cementite particles towards the network cementite existed throughout the entire coarsening process. We attribute the growth of the denuded zones to the

dissolution of small particles in the network vicinity due to this gradient.

B. Average Particle Size vs Time

The average particle diameter away from the denuded zones appeared to follow a power law relationship with time as shown in Figure 10. The trend lines for 1243 K and 1173 K (970 °C and 900 °C) passed through a common point at around $0.2 \mu\text{m}$ after 300 seconds of heat treatment. If the data point for 300 seconds at 1073 K (800 °C), which did not contain an IG distribution, was ignored (dotted line in Figure 10), the power law trend line for the 1073 seconds data also passed near $0.2 \mu\text{m}$ at that time.

As shown previously, there were multiple types of particles present in the steel samples (GB, IG, and LP). Thus, power law fits reflected apparent n values (n_{app}) relating to the fractions of each type of particle at a given time, rather than true n values relating to diffusion kinetics. Apparent n values (summarized in Table IV) from the power law trend lines in Figure 10 were 3.0 ± 0.3 at 1243 K (970 °C), 5.6 ± 0.8 at 1173 K (900 °C), and 10 ± 2 at 1073 K (800 °C). n_{app} values did not actually indicate coarsening mechanisms because they did not account for the effects of the multimodal particle size distribution. Since we have developed a means for separating particle types in the size distribution data, the next section assesses the growth kinetics for each particle type individually.

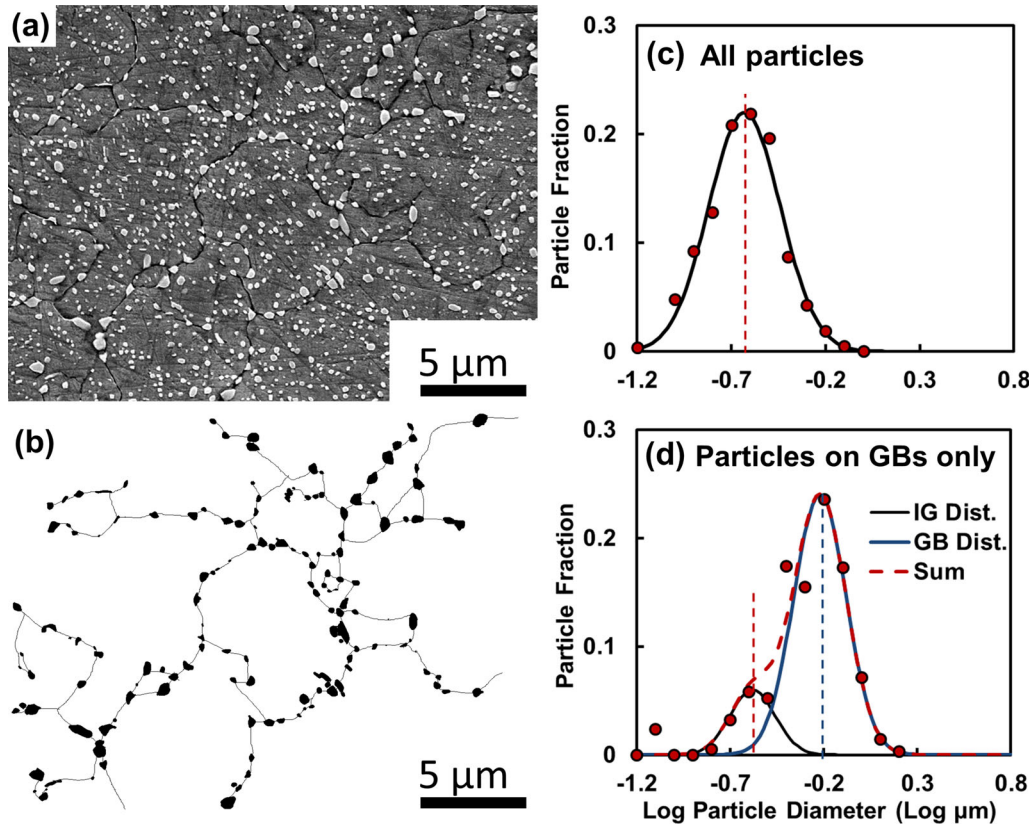


Fig. 9—Grain boundaries in (a) a micrograph of UHCS heat treated for 5 min at 1243 K (970 °C) were (b) traced to isolate particles on grain boundaries. Particle size distributions are shown for (c) all particles and (d) only particles at the identified grain boundaries.

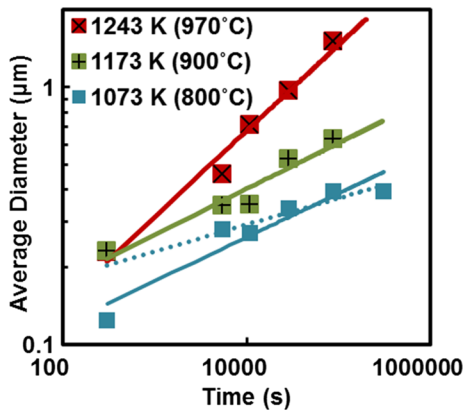


Fig. 10—Average particle diameter vs time. The dotted blue line shows the trend of average particle size at 1073 K (800 °C) excluding the data point at 300 s, which did not contain an IG peak.

C. Power Law Fits of Multimodal Distributions

The average values (peaks in the distributions) for the leftover (LP), intragranular (IG), and grain boundary (GB) particle size distributions were separated and plotted individually on log–log axes in Figure 11. Each point in Figure 11 was the center of one of the peaks in Figure 6. The power law fits to the data did not show any abrupt changes in slope. The exponents of the power law fits are labeled “ m ” and shown next to the corresponding power law fit trend lines. Apparent

$n = 1/m$ values (summarized in Table IV) were varied from 4 to 30. The apparent n values were only truly indicative of a rate-controlling diffusion mechanism if the effect of d_0^n was negligible for all data points. Extremely large values of n at 1073 K (800 °C) and for the intragranular particle data at 1173 K (900 °C) indicated that this was not the case at least for those datasets. Thus, n and k values from Figure 11 were also labeled n_{app} and k_{app} in Table IV. It was expected that the power law fit to the data at 1243 K (970 °C), having the fastest coarsening kinetics, would be least affected by d_0 and thus have n_{app} and k_{app} closest to the true values ($n \sim 5$ for intragranular particles and $n \sim 4$ for grain boundary particles). These n values are both similar to the $n = 4$ to 5 identified for denuded zone growth.

D. Accounting for Initial Particle Diameter

In order to find true n and k values, the effects of initial particle size d_0 on apparent rate of particle growth were addressed. d_0 and t_0 in the coarsening equation refer to the diameter and time, respectively at which steady-state coarsening begins. Since there were no apparent changes of slope in any of the power law fits in Figure 11, d_0 and t_0 were set based on the earliest time each type of distribution could be distinguished. With d_0 and t_0 thus defined, the equation $d^n - d_0^n = k_n(t - t_0)$ incorporated only two variables, n and k . For a prescribed n value (3, 4, or 5), it was possible to

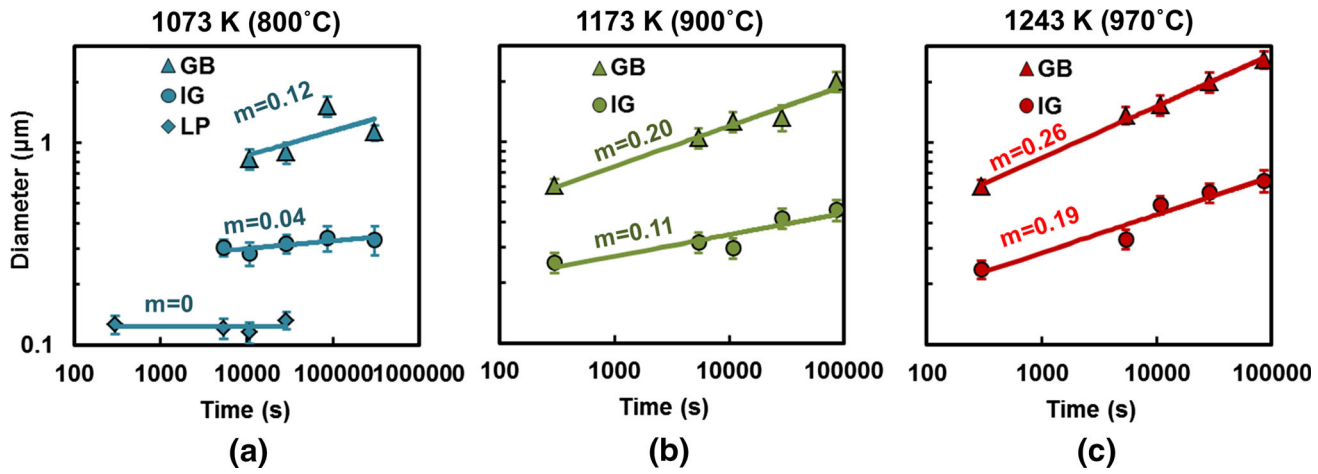


Fig. 11—Power law relationship of GB, IG, and LP particle diameters vs time for (a) 1073 K (800 °C), (b) 1173 K (900 °C), and (c) 1243 K (970 °C). m = exponent of the power law fit.

Table IV. Apparent n and k Values from Figs. 10 and 11 (Power Law Fits)

Temp	IG Particles		GB Particles		All Particles	
	$k_{\text{app}} (\mu\text{m}^n/\text{s})$	n_{app}	$k_{\text{app}} (\mu\text{m}^n/\text{s})$	n_{app}	$k_{\text{app}} (\mu\text{m}^n/\text{s})$	n_{app}
1243 K (970 °C)	1.2×10^{-6}	5.3 ± 0.8	5.1×10^{-4}	3.9 ± 0.1	3.1×10^{-5}	3.9 ± 0.1
1173 K (900 °C)	4.5×10^{-9}	9 ± 2	2.5×10^{-4}	4.9 ± 0.8	6.2×10^{-7}	5.6 ± 0.8
1073 K (800 °C)	5.3×10^{-19}	30 ± 10	3.0×10^{-5}	8 ± 7	3.8×10^{-8}	10 ± 2

determine a corresponding k by finding the slope of the line defined by $d^n - d_0^n$ vs $t - t_0$.

Figure 12(a) shows the possible k values for the intragranular particle coarsening at 1243 K (970 °C) determined by setting n equal to 3, 4, and 5. Figure 12 (b) shows different k values for the grain boundary particle coarsening at 1243 K (970 °C) determined by setting n equal to 3, 4, and 5. The coupled n and k values were also used to predict the mean particle size as a function of time, based on the equation:

$$d(t) = [k_n(t - t_0) + d_0^n]^{1/n}$$

The $d(t)$ values calculated in this manner were compared to the experimental datasets in log-log plots in Figures 12(c) and (d). Comparison of the values in Figure 12 showed that $n = 5$ provided the best fit to the measured data for IG particles, and $n = 4$ provided the best fit for GB particles (the red lines in Figures 12(c) and (d)). Volume diffusion appeared to be inhibited as a transport mechanism for coarsening inside the grains and on the grain boundaries, as $n = 3$ did not provide as good a fit to the data in both IG and GB cases.

Figures 13(a) and (b) show the possible k values for the IG and GB particle coarsening at 1173 K (900 °C) determined by setting n equal to 3, 4, and 5. The difference between the theoretical intragranular $d(t)$ lines calculated from each n and k combinations was smaller than at 1243 K (970 °C), and the relative effect of the scatter in the IG data was higher because the IG particle sizes were closer together. Nevertheless, $n = 5$ still

appeared to be the best fit to the data. In Figure 13(d), no GB data point could be determined at 300 seconds, so d_0 and t_0 were set at 5400 seconds instead. If GB particles existed in the samples at 1173 K (900 °C) after 300 seconds, they should certainly not be bigger than the size of the 1243 K (970 °C) GB particles at the same size. This size is marked in red in Figure 13(d). Note that the line which intersects the red point is closest to $n = 4$. Thus an n value close to 4 is most likely for the GB particle coarsening at 1173 K (900 °C).

Figures 14(a) and (b) show the possible k values for the IG and GB particle coarsening at 1073 K (800 °C) determined by setting n equal to 3, 4, and 5. The relative amount of scatter in the data in this case was high. The IG and GB k values were so small that there was very little difference in the $d(t)$ predictions based on the different n values. For this reason, Figures 14(c) and (d) show only one $d(t)$ line for $n = 3, 4, 5$. Since all mechanisms ($n = 3, 4, 5$) were compatible with the data, it was impossible to determine the most likely coarsening mechanism at 1073 K (800 °C) for both IG and BG particles. Though compatible with low k coarsening mechanisms, IG coarsening was still negligible at 1073 K (800 °C) over the time scale studied. GB coarsening on the other hand was non-negligible. Since the GB particles at higher temperatures [1173 K and 1243 K (900 °C and 970 °C)] were coarsened by a grain boundary mechanism ($n = 4$), we anticipate that the same mechanism was in operation at 1073 K (800 °C).

In summary, coarsening kinetics was analyzed assuming that intragranular particles and intergranular

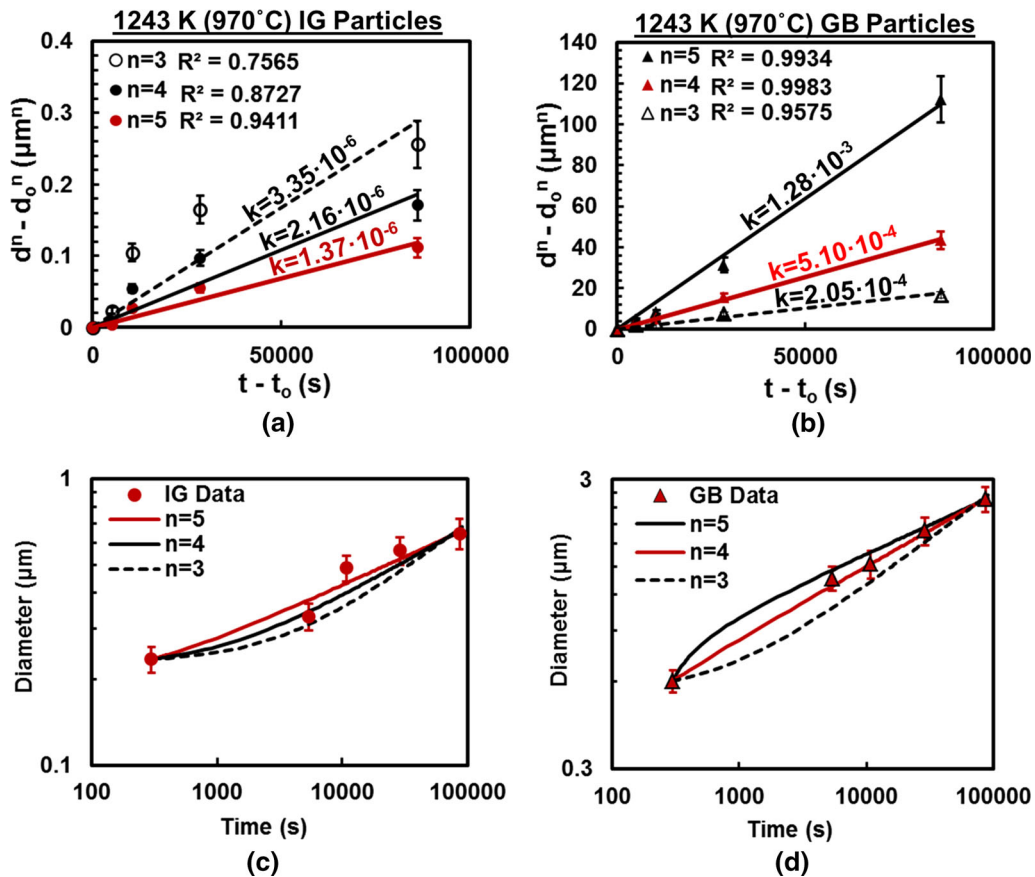


Fig. 12—1243 K (970 °C) plots of particle diameter and time to calculate k for (a) IG particles and (b) GB particles. Subsequently, k values were used to construct plots of theoretical d vs t for (c) IG and (d) GB particles (Color figure online).

particles coarsened independently. The values of coarsening exponent and rate constants are summarized in Table V. The data at all temperatures were consistent with $n = 4$ for GB particle coarsening, and $n = 5$ for IG particle coarsening, both of which are similar to the $n = 4$ to 5 observed in denuded zone growth adjacent to the cementite network. The values of the coarsening exponents at 1073 K (800 °C) have asterisks because any n of 3 to 5 was consistent with the data, and n values for IG and GB coarsening at that temperature were chosen assuming that the coarsening mechanism did not change over the temperature range studied. The n and k values at 1243 K (970 °C) in Table V are very similar to the n_{app} and k_{app} values at 1243 K (970 °C) from Table IV derived directly from $\log d$ vs $\log t$ plots, while values from the other temperatures differ significantly. Again, this is because d_0 became negligible quickly at 1243 K (970 °C) compared to the other temperatures. The coarsening exponent values for both IG and GB particles were consistent with the $n = 4$ to 5 which controlled denuded zone growth rate. Denuded zone growth should have involved both mechanisms, as both IG and GB particles near the proeutectoid cementite network would have to dissolve to form the denuded zones.

The coarsening exponent values of 4 and 5 found in this study were within the range seen in the literature, which reported n values from 3 to 5 at lower

temperatures, lower carbon content, and lower chromium content. However, this study may have been the first to find a coarsening exponent of 5 in association with IG particles alone. Lv *et al.* reported n values between 2 and 6 (including 5) in their study,^[24] but did not account for the possibility of multimodal particle distributions or possible effects of d_0 on the slopes of their log-log plots. In the literature, $n=3$ was always associated with coarsening of intragranular particles controlled by bulk diffusion and $n=4$ was always associated with coarsening controlled by grain boundary diffusion. Nam and Bae^[22] observed directly, and Day^[25] observed indirectly, that in simultaneous coarsening of IG and GB particles, IG particles were coarsened with $n=3$ and GB were coarsened with $n=4$. Excluding the study of Lv *et al.*, $n=5$ was only observed in one study by Lindsley and Marder,^[19] who theorized that it was associated with particle coarsening primarily on grain boundaries by a combined grain boundary and dislocation diffusion mechanism.

That n did not equal 3 for IG particles in this study was unexpected, especially since the temperatures we investigated were higher than the literature temperatures which should have encouraged bulk diffusion. The higher chromium content compared to the steels in the other literature studies may have been a factor leading to sluggish bulk diffusion. The high Cr composition may have lowered the effective diffusion coefficient for

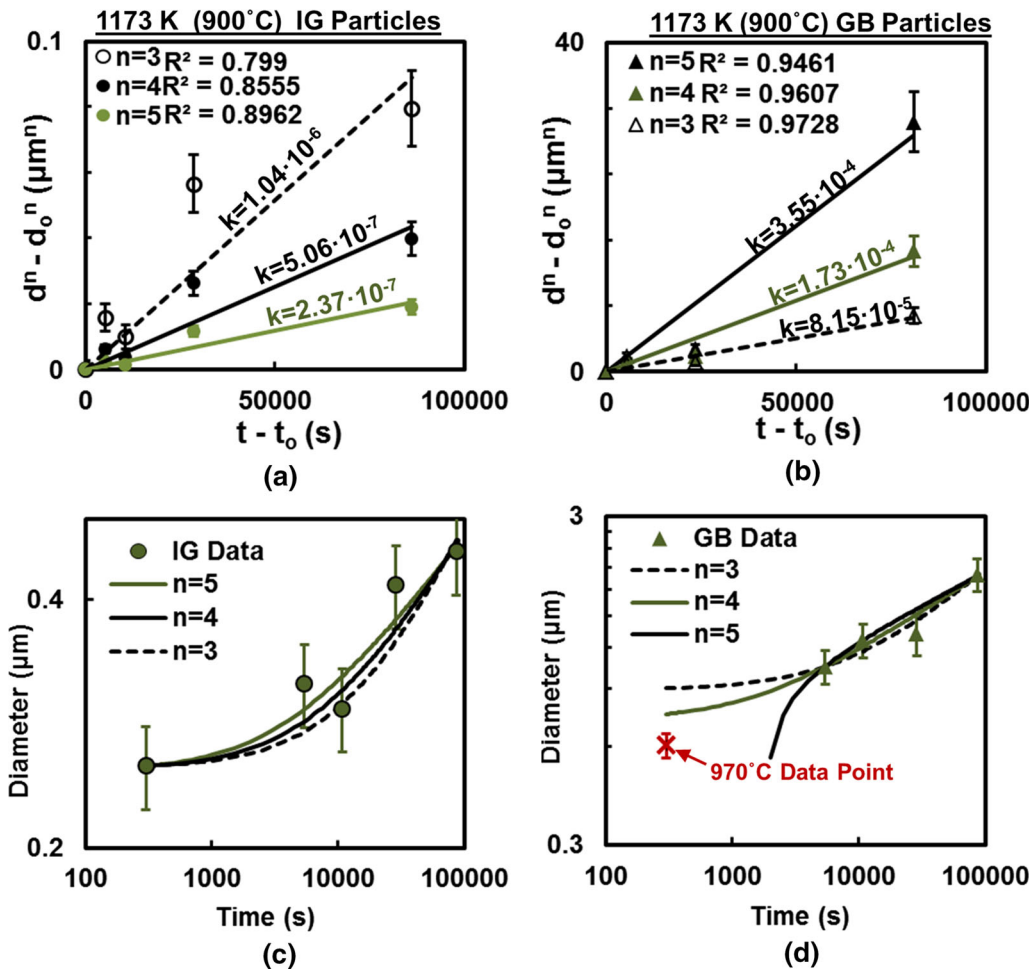


Fig. 13—1173 K (900 °C) plots of particle diameter and time to calculate k for (a) particles in the central peak (intragranular particles/IG) and (b) particles in the right peak (intergranular particles/GB). k values were used to construct plots of theoretical d vs t for (c) IG and (d) GB particles.

particle coarsening sufficiently for bulk diffusion to become slower than dislocation or grain boundary diffusion. We were unable to reliably calculate diffusion coefficients in this study to compare with the literature because of the high uncertainty in k values at 1173 K (900 °C) and especially at 1073 K (800 °C).

E. Time-Dependent Contributions of Each Coarsening Mechanism to Mean Particle Size

Figure 15 shows the fraction of GB and LP particles in this study plotted as a function of time. IG particle fractions are not shown because they can be found by subtracting GB and LP fractions from 1. Particle fractions were found by dividing the area under the corresponding peak by the sum of the areas under all peaks for a given time/temperature combination. Particle fractions exhibited a power law relation with time, consistent with Heckel's equations^[39] and observations^[40] relating the number of particles per volume N to a power of the coarsening time. The decrease in LP particle fraction with time, $f_{LP} = 64t^{-0.7}$ was due to LP particle dissolution as well as IG particle formation from pearlite spheroidization. The increase in GB

particle fraction with time, $f_{GB} = kt^{0.4-0.5}$, was primarily due to IG particle dissolution.

The contribution of each particle distribution to the mean particle size in the steel was determined using the fractions of the distributions made up of IG and GB particles. The contributions of each particle distribution A were determined as follows:

$$C_A(t) = f_A(t) [k_A(t - t_{0A}) + d_{0A}^n]^{1/n}.$$

For example, at 1243 K (970 °C) the two contributions would be:

$$\text{GB contribution : } (0.002 \cdot t^{0.493}) \cdot [5.1 \times 10^{-4} \cdot (t - 300) + 0.60^4]^{1/4}$$

$$\text{IG contribution : } (1 - 0.002 \cdot t^{0.493}) \cdot [1.4 \times 10^{-6} \cdot (t - 300) + 0.23^5]^{1/5}$$

Contributions from each particle distribution were calculated for 1073 K (800 °C), 1173 K (900 °C), and

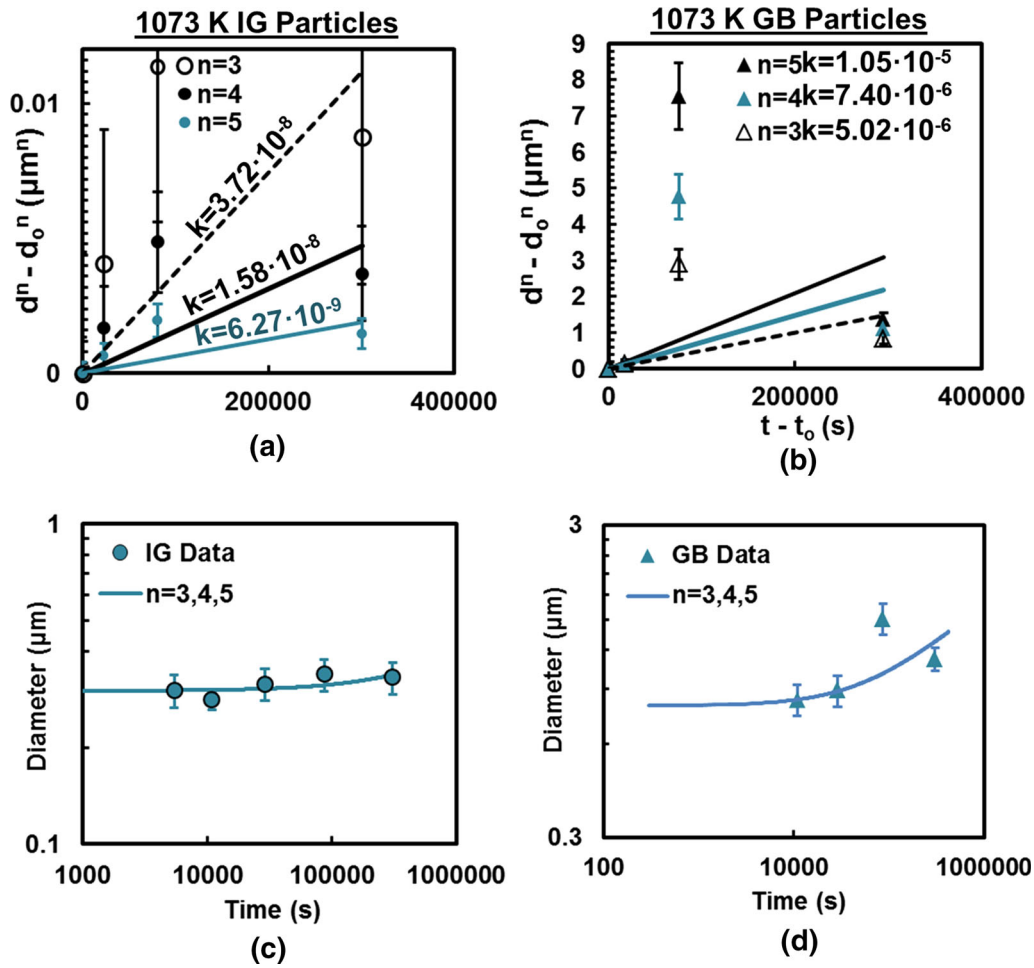


Fig. 14—1073 K (800 °C) plots of particle diameter and time to calculate k for (a) particles in the central peak (intragranular particles/IG) and (b) particles in the right peak (intergranular particles/GB). k values were used to construct plots of theoretical d vs t for (c) IG and (d) GB particles.

Table V. n and k Values from Figs. 12, 13, and 14

Temp	IG Particles		GB Particles	
	k ($\mu\text{m}^5/\text{s}$)	n	k ($\mu\text{m}^4/\text{s}$)	n
1243 K (970 °C)	1.4×10^{-6}	5	5.1×10^{-4}	4
1173 K (900 °C)	2.4×10^{-7}	5	1.7×10^{-4}	4
1073 K (800 °C)	6.2×10^{-9}	5*	7.4×10^{-6}	4*

*The data were consistent with any $n=3$ to 5 for coarsening at 1073 K (800 °C). n values were assumed to stay consistent with the other n values in the range of temperatures studied.

1243 K (970 °C). The sums of the contributions were then compared to the measured mean particle size data in Figure 16. At 1073 K (800 °C), IG particles were the main contributors to mean particle size except for short heating times when the LP particle contribution was important (Less than ~5400 seconds). At long heating times (greater than about 8 hours), the GB contribution to mean particle size had become noticeable. By extrapolation, GB particles should become the primary contributors to mean particle size after holding around

500 hours at 1073 K (800 °C). At 1173 K (900 °C) IG particles were the main contributors to mean particle for the entire time range that was studied. The influence of GB particles on the mean particle diameter became noticeable after around 3 hours of heat treatment. GB particles should become the primary contributors to mean particle size after around 58 hours of heating at 1173 K (900 °C). At 1243 K (970 °C), the contribution of GB particles to mean particle size was noticeable after only 90 minutes. GB particles became the primary

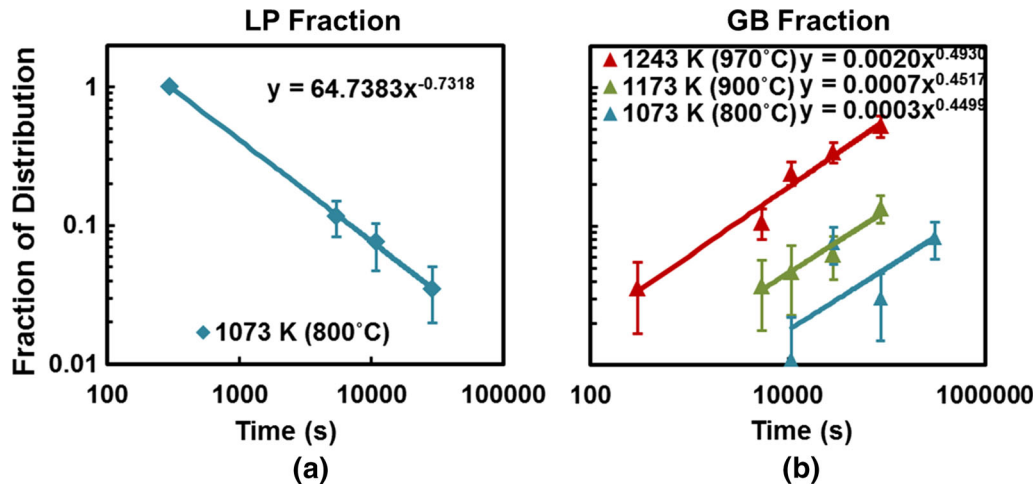


Fig. 15—Time evolution of the fractions of particles which make up (a) preexisting particle (LP) peak at 1073 K (800 °C), and (b) the grain boundary (GB) particle peaks at 1073 K, 1173 K, and 1243 K (800 °C, 900 °C, and 970 °C).

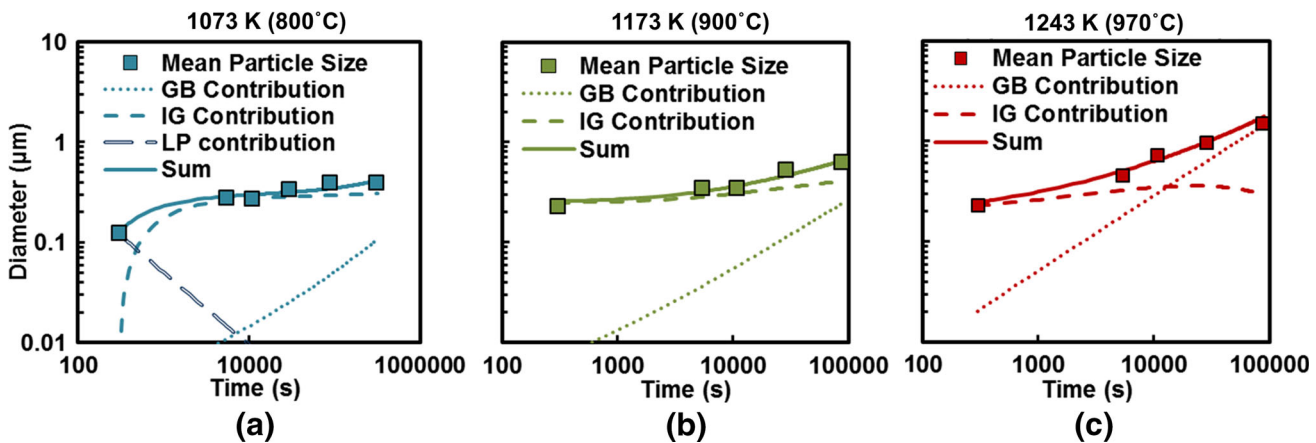


Fig. 16—Contributions from IG, GB, and LP particle distributions at (a) 1073 K (800 °C), (b) 1173 K (900 °C), and (c) 1243 K (970 °C) were summed to find a theoretical mean particle size as a function of time, which was compared to the measured mean particle sizes.

contributors to mean particle size after about 3 hours of heat treatment at 1243 K (970 °C).

The results of this study show how elevated temperature annealing could be used as a tool to modify room-temperature UHCS microstructures. Longer heat treatments and higher temperatures increased the particle fraction and mean size of large GB particles as well as the size of the denuded zones next to the cementite network. Both effects would promote pearlite formation after the heat treatment by increasing the particle spacing and making the divorced eutectoid transformation less likely. Shorter heat treatment times at lower temperatures would have the opposite effect and promote a finer particle distribution with less pearlite.

V. CONCLUSIONS

An initially pearlitic UHCS containing a cementite network was heat treated at 1073 K, 1173 K, and 1243 K (800 °C, 900 °C, and 970 °C) for times of 5 minutes to

24 hours. The pearlite quickly spheroidized into carbide particles, which then coarsened over time. A denuded zone devoid of particles developed adjacent to branches of the preexisting proeutectoid cementite network. Denuded zone width evolved with time described by the equation $d^{4-5} = kt$ (d in μm). We theorized that the exponent for growth of the denuded zone was related to the exponents controlling particle coarsening.

Away from the denuded zone, particle size distributions were clearly multimodal. Three-component distributions were identified, corresponding to different types of particles: medium-sized intragranular (IG) particles around $0.2 \mu\text{m}$ and larger produced by pearlite spheroidization inside austenite grains; larger grain boundary (GB) particles around $0.6 \mu\text{m}$ and larger; and very small leftover particles (LP) around $0.13 \mu\text{m}$ in size that formed in the casted UHCS prior to annealing. GB particle distributions were confirmed by tracing along prior austenite grain boundaries and retaining only the GB distribution. LP distributions were attributed to preexisting divorced pearlite or possibly to preexisting M_{23}C_6 .

Plotting the mean diameter of all particles within each sample vs time on log-scale axes resulted in apparent power law relations which were without meaning due to the multimodal distributions. When the individual IG and GB distributions were plotted on log-log axes, apparent n values were much larger than the true n values for the distributions at 1173 K and 1073 K (900 °C and 800 °C) due to the influence of the initial particle size d_0 . 1243 K (970 °C) n and k values were close to the true values because k was large enough that d_0 became negligible very quickly. In order to identify the true n and k values for the distributions, k was fixed for each n value by plotting $d^n - d_0^n$ vs $t - t_0$ for n values of 3, 4, and 5. The resulting $d(t)$ lines for each n and k pair were compared to the data.

We determined that the most likely value of n for IG particles was five at all temperatures studied, indicating coarsening controlled by diffusion along dislocations. Chromium alloying in the steel may have significantly decreased the effective diffusion coefficient, retarding volumetric diffusion. IG particles at 1073 K (800 °C) displayed negligible coarsening. The most likely value of n for GB particles was four at all temperatures studied, indicating coarsening controlled by diffusion along grain boundaries. Coarsening exponents of IG and GB particles were consistent with the $n = 4$ to 5 range found in the power law rate of denuded zone growth.

The fraction of the distribution corresponding to the GB particles at all temperatures and LP particles at 1073 K (800 °C) was determined to be power law functions of time. The GB fraction increased with time according to $f_{GB} = kt^{4.5-5}$. The LP fraction decreased with time according to $f_{LP} = 64t^{-0.7}$. GB and LP fractions were used to calculate contributions of each type of particle to the overall mean particle sizes. It was determined that GB particles became the primary contributors to overall mean particle sizes at about 500 hours of heat treatment at 1073 K (800 °C) (projected), 58 hours at 1173 K (900 °C), and 3 hours 1243 K (970 °C). Overall, carbide particle size quantification from digital micrographs in relation to existing microstructural features, like prior austenite grain boundaries and proeutectoid cementite network, allowed evaluation of multimodal carbide particle coarsening kinetics.

ACKNOWLEDGMENTS

The authors appreciate Miller Centrifugal Casting for providing as-cast mill roll parts for this study, as well as their insightful discussions. This project was financed in part by a grant from the Commonwealth of Pennsylvania Department of Community and Economic Development (DCED), Developed in PA Program (D2PA). Funding support is also acknowledged from the National Science Foundation, CMMI Award No. 1436064. The authors acknowledge the use of the Materials Characterization Facility at Carnegie Mellon University supported by grant MCF-677785.

REFERENCES

1. J.R. Speer and W.L. Forster: *US Pat. 1,346,343*, 1913.
2. D.R. Lesuer, C.K. Syn, and O.D. Sherby: *Ultrahigh Carbon Steel for Automotive Applications*, SAE Technical Paper 960314, 1996.
3. D.R. Lesuer, C.K. Syn, A. Goldberg, J. Wadsworth, and O.D. Sherby: *JOM*, 1993, vol. 45, pp. 40–46.
4. M.D. Hecht, B.A. Webler, and Y.N. Picard: *Mater. Charact.*, 2016, vol. 117, pp. 134–43.
5. M.A. Hamidzadeh, M. Meratian, and A. Saatchi: *Mater. Sci. Eng. A*, 2013, vol. 571, pp. 193–98.
6. K.P. Liu, X.L. Dun, J.P. Lai, and H.S. Liu: *Mater. Sci. Eng. A*, 2011, vol. 528, pp. 8263–68.
7. M.A. Hamidzadeh, M. Meratian, and M. Mohammadi Zahrani: *Mater. Sci. Eng. A*, 2012, vol. 556, pp. 758–66.
8. A. Fernández-Vicente, M. Carsi, F. Penalba, E. Taleff, and O.A. Ruano: *Mater. Sci. Eng. A*, 2002, vol. 335, pp. 175–85.
9. S.P. Rawal and J. Gurland: *Metall. Trans. A*, 1977, vol. 8, pp. 691–98.
10. C.K. Syn, D.R. Lesuer, and O.D. Sherby: *Metall. Mater. Trans. A*, 1994, vol. 25A, pp. 1481–93.
11. J. Gurland: *Acta Metall.*, 1972, vol. 20, pp. 735–41.
12. *Rolls for the Metalworking Industries*, ed., Gene.E. Lee, ed., *Rolls for the Metalworking Industries*, Iron and Steel Society, Warrendale, PA, 2002.
13. J.D. Verhoeven and E.D. Gibson: *Metall. Mater. Trans. A*, 1998, vol. 29A, pp. 1181–89.
14. I.M. Lifshitz and V.V. Slyozov: *J. Phys. Chem. Solids*, 1961, vol. 19, pp. 35–50.
15. C. Wagner: *Zeitschrift Für Elektrochemie*, 1961, vol. 65, pp. 581–91.
16. M. Kahlweit: *Adv. Colloid Interface Sci.*, 1975, vol. 5, pp. 1–35.
17. M.V. Speight: *Acta Metall.*, 1968, vol. 16, pp. 133–35.
18. A.J. Ardell: *Acta Metall.*, 1972, vol. 20, pp. 601–09.
19. B.A. Lindsley and A.R. Marder: *Acta Mater.*, 1998, vol. 46, pp. 341–51.
20. P. Deb and M.C. Chaturvedi: *Metallography*, 1982, vol. 354, pp. 41–54.
21. A.R. Marder and B.L. Bramfitt: *Metall. Trans. A*, 1975, vol. 6, pp. 2009–14.
22. W.J. Nam and C.M. Bae: *Scripta Mater.*, 1999, vol. 41, pp. 313–18.
23. A.M. Cree, R.G. Faulkner, and A.T. Lyne: *Mater. Sci. Technol.*, 1995, vol. 11, pp. 566–71.
24. Z.Q. Lv, S.H. Sun, Z.H. Wang, M.G. Qv, P. Jiang, and W.T. Fu: *Mater. Sci. Eng. A*, 2008, vol. 489, pp. 107–12.
25. R.V. Day and J. Barford: *Nature*, 1968, vol. 217, pp. 1145–46.
26. C.-Y. Li, J. Blakely, and A. Feingold: *Acta Metall.*, 1966, vol. 14, pp. 1397–402.
27. L. Richard and G. Krauss: *Metall. Trans. A*, 1976, vol. 7, pp. 983–89.
28. A.A. Vasilyev, S.F. Sokolov, N.G. Kolbasnikov, and D.F. Sokolov: *Phys. Solid State*, 2011, vol. 53, pp. 2194–200.
29. G.H. Zhang, J.Y. Chae, K.H. Kim, and D.W. Suh: *Mater. Charact.*, 2013, vol. 81, pp. 56–67.
30. J.O. Andersson, T. Helander, L. Höglund, P. Shi, and B. Sundman: *Calphad*, 2002, vol. 26, pp. 273–312.
31. F.S. Birks, N. Meier, and G.H. Pettit: *Introduction to the High Temperature Oxidation of Metals*, 2nd ed., Cambridge University Press, 2006.
32. C.A. Schneider, W.S. Rasband, and K.W. Eliceiri: *Nat. Methods*, 2012, vol. 9, pp. 671–75.
33. S.A. Saltikov: in *Proc. Second Int. Congr. Stereol.*, Hans Elias, ed., Springer, Chicago, 1967, pp. 163–73.
34. D.L. Sahagian and A.A. Proussevitch: *J. Volcanol. Geotherm. Res.*, 1998, vol. 84, pp. 173–96.
35. E. Limpert, WA Stahel, and M Abbt: *Bioscience*, 2001, vol. 51, p. 341.
36. J. Heintzenberg: *Aerosol Sci. Technol.*, 1994, vol. 21, pp. 46–48.
37. D.P. Yao, Y.Z. Zhang, Z.Q. Hu, Y.Y. Li, and C.X. Shi: *Scripta Metall.*, 1989, vol. 23, pp. 537–41.
38. T. Krol, D. Baither, and E. Nembach: *Acta Mater.*, 2004, vol. 52, pp. 2095–2108.
39. R.W. Heckel: *Trans. Am. Soc. AIME*, 1965, vol. 233, pp. 1994–2000.
40. K.M. Vedula and R.W. Heckel: *Metall. Trans.*, 1970, vol. 1, pp. 9–18.